Article

Analysis of Phase Diagram of $CaO\text{-}CoO_x\text{-}ErO_y$ and Crystal Structure of Perovskite $(Ca_{3-x}Er_x)Co_2O_{6-z}$ Solid Solution

HaoCheng Wang [1,△], HaoMing Ning [1,△], ZhenJun Fan [1,*] and GuangYao Liu [2,*]

[1] School of Science, China University of Geosciences Beijing, Beijing, 100083, China
[2] China University of Geosciences Beijing, Beijing, 100083, China
△ The co-first author
* Corresponding author, E-mail address: fanzj@cugb.edu.cn (Z.F.) ; guangyaoliu@hotmail.com (G.L.)

Abstract: In this work, a series of compounds in the $CaO\text{-}CoO_x\text{-}ErO_y$ ternary oxide system were synthesized in air at 885 ℃ using high temperature solid-phase synthesis method. Phase boundary of each solid solution region in the $CaO\text{-}CoO_x\text{-}ErO_y$ system was determined by X-ray powder diffraction technique. The phase diagram of the $CaO\text{-}CoO_x\text{-}ErO_y$ system at 885 ℃ includes three series of ternary oxide solid solutions : $(Ca_{3-x}Er_x)Co_4O_{9-z}$ ($0\le x\le 0.9$), $(Ca_{3-x}Er_x)Co_2O_{6-z}$ ($0\le x\le 1.25$) and $(Er_{1-x}Ca_x)CoO_{3-z}$ ($0\le x\le 0.33$). Four three-phase regions and five solid solution tie-line regions were obtained. The structure of perovskite solid solution $(Ca_{3-x}Er_x)Co_2O_{6-z}$ has been analyzed by Rietveld refinements. With the increase of Er content, the cell parameters of $(Ca_{3-x}Er_x)Co_2O_{6-z}$ exhibit an decreasing trend in *a* and *b* directions and an increasing trend in *c* direction. A brief comparison of the phase diagrams of the $CaO\text{-}CoO_x\text{-}RO_y$ (R=La, Dy, and Er) systems in air at 885 ℃ is given.

Keywords: Phase diagram of $CaO\text{-}CoO_x\text{-}ErO_y$ system; Thermoelectric oxide system; Perovskite and its derived structures; Structure for $(Ca_{3-x}Er_x)Co_2O_{6-z}$

1. Introduction

The increasing demand for energy in everyday life, coupled with concerns about climate change, has prompted the scientific community to explore materials for more efficient energy conversion and storage. Perovskite [1-3] is a kind of outstanding materials, including metal halides and perovskite oxides, which has a good development prospect as energy materials and can effectively replace traditional materials. In 1839, Russian geologist Lev Perovski discovered the structure of ABO_3. Because the perovskite structure was generated by the discovery of the special structure of $CaTiO_3$ in calcium titanate during the study of perovskite, the structure of ABO_3 is called the perovskite structure. The perovskite structure is also called the 113 structure because the proportion of the elements in ABO_3 is A:B:O=1:1:3. The spatial group of the standard perovskite structure is P m3m. In ABO_3, A is a alkaline earth metal or rare earth ion with a relatively large ionic radius, B is a transition metal ion with a relatively small ionic radius, and O is oxygen ion [4,5].

In recent years, perovskite-type thermoelectric materials have made breakthrough progress, but only a few of them have been found to have practical industrial applications due to the low efficiency. To measure the performance of thermoelectric materials the dimensionless figure of merit (zT), given by $zT=S^2\sigma T/\kappa$ [6-8], where S is the Seebeck coefficient or thermopower, σ is the electrical conductivity ($\sigma=1/\rho$, ρ is electrical resistivity), κ is the thermal conductivity, and T is the absolute temperature, has been used. However, due to the correlation of S, ρ and κ, it is a difficult task to optimize the zT value. High quality thermoelectric materials need to meet the following requirements: high electrical conductivity, high Seebeck coefficient, and low thermal conductivity.

Thermoelectric oxides have been considered as possible candidates for waste heat conversion applications because of their stability at high temperatures. Low-dimensional oxide thermoelectric materials, including chain oxides $Ca_3Co_2O_6$ [9-11] and layered oxides $Ca_3Co_4O_9$ [12-20], $NaCo_2O_4$ [21], $Bi_2Sr_2Co_2O_x$ [22] and natural superlattices (Bi,A)OCuSe (A=Pb, Ba, Sr, Ca) [23], are considered as

Preprints (www.preprints.org) | NOT PEER-REVIEWED | Posted: 22 May 2023 doi:10.20944/preprints202305.1486.v1

candidates for waste heat conversion applications. Among them, the 2D mismatched layered oxide $Ca_3Co_4O_9$ exhibited the highest *ZT* value. Much work has been done to improve the thermoelectric properties of $Ca_3Co_4O_9$ by doping at Ca or Co sites [24-27].

Phase equilibrium diagrams which provide blue prints for processing and understanding phase relationships are important for designing and understanding materials properties, phase diagrams of the CaO-CoO_x-RO_y (R=lanthanide) systems are of interest to the thermoelectric research community. Phase diagrams of CaO-CoO_x-RO_y systems for R= La [28], Nd [29], Sm [30], Eu [31], Gd [32], Dy [33]and Ho [34] have been reported. In the CaO-CoO_x-RO_y system, there are $Ca_3Co_4O_9$, $Ca_3Co_2O_6$ and $RCoO_3$ phases, all of which have perovskite or its derivative structure and have excellent thermoelectric properties.

In this study, we have established the phase compatibility relationships, crystal chemistry, and crystallography of selected compounds in the CaO-CoO_x-RO_y systems at 885 ℃ (R=Er in this report), particularly to obtain subsolidus phase relationships in the vicinity of the $Ca_3Co_4O_9$ and $Ca_3Co_2O_6$ compounds. Possible formation of $(Ca_{3-x}Er_x)Co_4O_{9-z}$, $(Er_{1-x}Ca_x)CoO_{3-z}$ and $(Ca_{3-x}Er_x)Co_2O_{6-z}$ solid solutions and the effect of doping on the crystal structure are also discussed. In addition, the phase formation and phase relationships between CaO-CoO_x-LaO_y [28], CaO-CoO_x-DyO_y [33], and the CaO-CoO_x-ErO_y systems are compared. These reference patterns will be included in the ICDD Powder Diffraction File (PDF [35]).

2. Materials and Methods

2.1. Sample preparation

The samples were prepared by high temperature solid-state synthesis technique. **Table 1** gives 52 samples prepared from stoichiometric mixtures of $CaCO_3$, Co_3O_4 and Er_2O_3 (all with purity greater than 99%). The samples were mixed, pelletized, and sintered at 850 ℃ for 6 hours, its purpose is to calcinate $CaCO_3$ at high temperature and react $CaCO_3$ into CaO. The samples are ground repeatedly, the particles are small after grinding, and the samples are mixed evenly. They were then sintered at 885 ℃ for 6-9 days, with grinding, and the heat treatment process repeated until the powder X-ray diffraction pattern showed no further change.

Table 1. Fifty-two samples (mole fraction, %) prepared for the phase equilibria study of the CaO-CoO_x-ErO_y system at 885 °C in air. In this table, Ca=CaO; Co=⅓Co_3O_4; Er=½Er_2O_3.

Sample#	Ca	Co	Er
#01	0.05	0	0.95
#02	0.08	0	0.92
#03	0.1	0	0.9
#04	0.95	0	0.05
#05	0.98	0	0.02
#06	0.05	0.2	0.75
#07	0.2	0.2	0.6
#08	0.55	0.24	0.21
#09	0.65	0.25	0.1
#10	0	0.3333	0.6667
#11	0.3	0.3333	0.3667
#12	0.31	0.3333	0.3567
#13	0.32	0.3333	0.3467
#14	0.3333	0.3333	0.3334
#15	0.35	0.3333	0.3167

Preprints (www.preprints.org) | NOT PEER-REVIEWED | Posted: 22 May 2023 doi:10.20944/preprints202305.1486.v1

#16	0.39	0.3333	0.2767
#17	0.4	0.3333	0.2667
#18	0.42	0.3333	0.2467
#19	0.43	0.3333	0.2367
#20	0.45	0.3333	0.2167
#21	0.5	0.3333	0.1667
#22	0.55	0.3333	0.1167
#23	0.4	0.4	0.2
#24	0.5	0.4	0.1
#25	0.55	0.4	0.05
#26	0.6	0.4	0
#27	0.2	0.425	0.375
#28	0	0.5	0.5
#29	0.1	0.5	0.4
#30	0.15	0.5	0.35
#31	0.16	0.5	0.34
#32	0.17	0.5	0.33
#33	0.18	0.5	0.32
#34	0.19	0.5	0.31
#35	0.2	0.5	0.3
#36	0.21	0.5	0.29
#37	0.22	0.5	0.28
#38	0.25	0.5	0.25
#39	0.28	0.5	0.22
#40	0.3	0.5	0.2
#41	0.25	0.5714	0.1786
#42	0.26	0.5714	0.1686
#43	0.27	0.5714	0.1586
#44	0.28	0.5714	0.1486
#45	0.29	0.5714	0.1386
#46	0.295	0.5714	0.1336
#47	0.3	0.5714	0.1286
#48	0.3572	0.5714	0.0714
#49	0.4143	0.5714	0.0143
#50	0.4286	0.5714	0
#51	0.02	0.6	0.38
#52	0.2	0.65	0.15

2.2. X-ray diffraction

X-ray powder diffraction (XRD) analysis of the samples has been carried out at room temperature using a Rigaku SmartLab diffractometer with Cu K_α radiation (40 kV, 200 mA) and a graphite monochromator at the China University of Geosciences Beijing. A step scan mode was employed with a step width of $2\theta=0.02°$ and a sampling time of 1 s in the range of $15\leq 2\theta \leq 70°$. The

Preprints (www.preprints.org) | NOT PEER-REVIEWED | Posted: 22 May 2023 doi:10.20944/preprints202305.1486.v1

compositions in the CaO-CoO_x-ErO_y system were analyzed by using the Powder Diffraction File (PDF) [35].

2.3. Rietveld refinements

The structural changes of the samples in the solid solution region $(Ca_{3-x}Er_x)Co_2O_{6-z}$ were analyzed by Rietveld refinements [36,37]. X-ray powder diffraction (XRD) analysis of these perovskite crystals has been carried out at room temperature using a Rigaku SmartLab diffractometer with Cu K_α radiation (40 kV, 200 mA) and a graphite monochromator as mentioned above. A step scan mode was employed with a step width of $2\theta=0.02°$ and a sampling time of 1 s in the range of $15\leq 2\theta\leq 120°$.

3. Results

Figure 1 shows the phase diagram of the CaO-CoO_x-ErO_y system that was determined at 885 ℃. The phase relations between the solid solution and other phases are represented by tie-lines. The phase diagram of CaO-CoO_x-ErO_y ternary system at 885℃ has 5 two-phase zones, 4 three-phase zones, 8 two-phase contact lines and 3 solid solution zones. The phase diagram of CaO-CoO_x-ErO_y ternary system at 885℃ shows three solid solution distinctions: $(Ca_{3-x}Er_x)Co_4O_{9-z}$ $(0\leq x\leq 0.9)$, $(Ca_{3-x}Er_x)Co_2O_{6-z}$ $(0\leq x\leq 1.25)$ and $(Er_{1-x}Ca_x)CoO_{3-z}$ $(0\leq x\leq 0.33)$. The crystal chemistry and crystallography of the phases in binary and ternary oxide systems are discussed below.

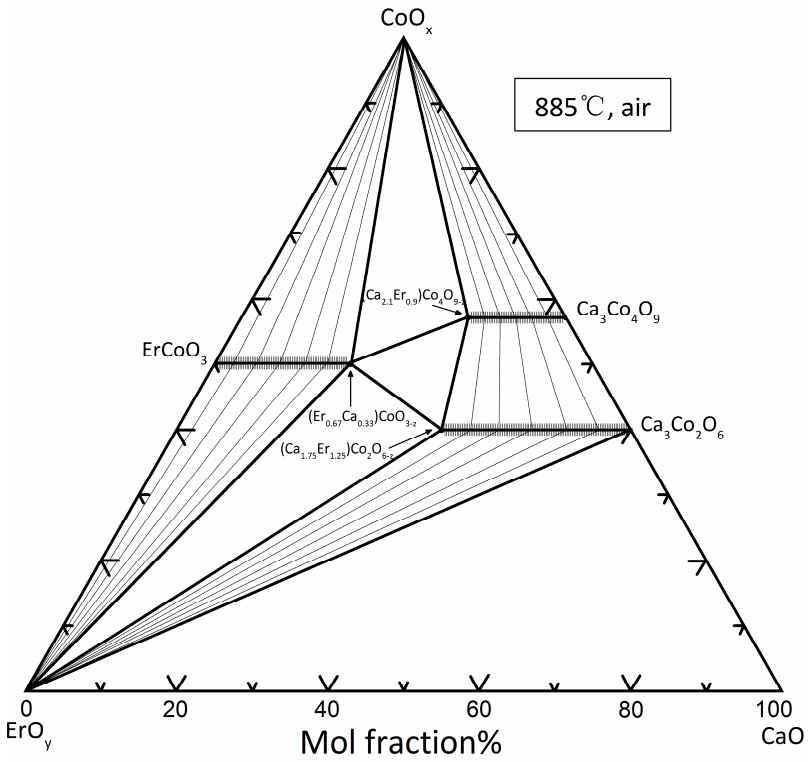

Figure 1. Phase diagram of the CaO-CoO_x-ErO_y system at 885℃ in air, showing the limits of various solid solutions, and the tie-line relationships of various phases.

3.1. Binary oxide systems

3.1.1. CaO-CoO_x

Binary CaO-CoO_x oxide systems have been studied extensively. In this system, two single-phase structures have been identified: $Ca_3Co_2O_6$ (Co:Ca=40:60) and $Ca_3Co_4O_9$ (Co:Ca=57.14:42.86) [12,24]. Both $Ca_3Co_2O_6$ and $Ca_3Co_4O_9$ have perovskite-derived structures. It is also confirmed that there are only two single-phase $Ca_3Co_2O_6$ and $Ca_3Co_4O_9$ in the binary system under the current high temperature solid-phase synthesis conditions.

Preprints (www.preprints.org) | NOT PEER-REVIEWED | Posted: 22 May 2023 doi:10.20944/preprints202305.1486.v1

$Ca_3Co_4O_9$ is a mismatched layered oxide with two monocline subsystems, with the same a, c, but different b values. There are two different Co-O layers stacked regularly along the direction of the c-axis, one of which is CoO_2 layer, CoO_2 layer has a CdI_2-type structure, CoO_2 layer can be regarded as Co ion in the center, there are six O ions around the central Co ion, the center of the octahedron is Co ion, the apex of the octahedron is O ion. Adjacent octahedrons are connected in the form of common edges; The other layer is Ca_2CoO_3, formed from Ca-Co-O, which has a halite structure. CoO_2 layer can provide charge carriers (holes) needed for conducting electricity, and Co ions in CoO_2 layer include Co^{3+} and Co^{4+}, located at the adjacent O^{2-} midpoint. There is strong interaction between adjacent positive ions. The change of valence of Co ion makes it easy to shift from the center of the octahedron, resulting in the difference in the length of Co-O bond. The bonding mode between ions in Ca_2CoO_3 layer is ionic bond, and there is no change of valence, so Ca_2CoO_3 layer does not conduct electricity, and the presence of Ca_2CoO_3 reduces the thermal conductivity of the material. Higher conductivity σ and lower thermal conductivity κwill make the material have higher thermoelectric value. Therefore, the phase exhibits strong anisotropic thermoelectric properties in the ab plane [33].

$Ca_3Co_2O_6$ (R -3c, a=9.0793 (7) Å, c=10.381 (1) Å) is a member of the n=1 of the perovskite-derived series $A_{n+2}B_nB'O_{3n+3}$, where the A positions are alkaline earth metals, such as Ca, Sr and Ba, and the B and B' positions are usually transition metal elements. In $Ca_3Co_2O_6$, the A site is the Ca ion, the B site is the Co ion in the center of the octahedron, and the B 'site is the Co ion in the center of the distorted trigonal prism [34]. **Figure 2** shows the structure of $Ca_3Co_2O_6$. $Ca_3Co_2O_6$ has a one-dimensional Co-O chain structure. This unique structure makes $Ca_3Co_2O_6$ obtain excellent thermoelectric properties, magnetic properties and chemical stability. $Ca_3Co_2O_6$ is suitable for use in moderate and relatively harsh environmental conditions. The Seebeck coefficient of $Ca_3Co_2O_6$ increases with the increase of temperature, the conductivity of $Ca_3Co_2O_6$ is semiconductor, and the thermal conductivity of $Ca_3Co_2O_6$ is relatively low. Therefore, $Ca_3Co_2O_6$ is a kind of high efficient thermoelectric material with potential to be developed.

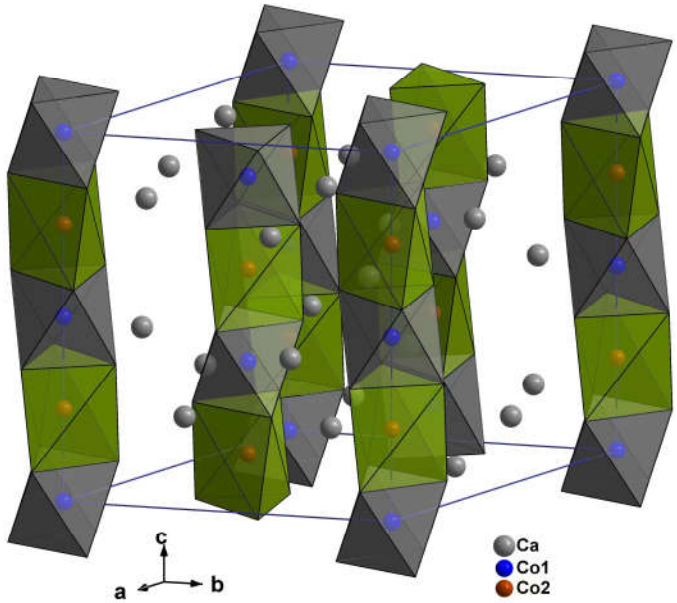

Figure 2. Crystal structure of $Ca_3Co_2O_6$ showing the linear chain characteristics of Co-O octahedron and Co-O prism, each $Co_2O_6^{6-}$ chain is surrounded by six other chains. These $Co2O6^{6-}$ chains are separated by octa-coordinated Ca^{2+} ions.

3.1.2. $CaO\text{-}ErO_y$

Five samples were prepared in the $CaO\text{-}ErO_y$ binary system to determine the phases form. There is no single phase in the $CaO\text{-}ErO_y$ binary system, indicating that there is no solid solution near CaO and Er_2O_3, that is, there is no solid solution zone in the $CaO\text{-}ErO_y$ binary system.

Preprints (www.preprints.org) | NOT PEER-REVIEWED | Posted: 22 May 2023 doi:10.20944/preprints202305.1486.v1

3.1.3. CoO_x-ErO_y

At 885 ℃, the only phase found in the ErO_x-CoO_y system is the $ErCoO_3$ phase, which has the P nma space group perovskite structure. In the CoO_x-LaO_y binary system of the CaO-CoO_x-LaO_y [28] phase diagram, La_2CoO_4 phase was determineds, but in this study the Er_2CoO_4 phase could not be prepared under the present conditions.

3.2. Ternary oxide systems

Three series of ternary solid solutions were found at 885℃, which were $(Ca_{3-x}Er_x)Co_4O_{9-z}$ ($0\leq x\leq 0.9$), $(Ca_{3-x}Er_x)Co_2O_{6-z}$ ($0\leq x\leq 1.25$) and $(Er_{1-x}Ca_x)CoO_{3-z}$ ($0\leq x\leq 0.33$). We found the solid solution region $(Ca_{3-x}Er_x)Co_4O_{9-z}$ near $Ca_3Co_4O_9$ and the solid solution region $(Er_{1-x}Ca_x)CoO_{3-z}$ near $ErCoO_3$ are close to the previously reported range in the other CaO-RO_x-CoO_y systems. The solution region $(Ca_{3-x}Er_x)Co_2O_{6-z}$ was found near $Ca_3Co_2O_6$, while the solid solution of other lanthanides did not occur at $(Ca,R)_3Co_2O_6$. Different from the CaO-CoO_x-RO_y (R=Eu, Gd, Sm) systems as reported previously, the solid solution region of $(Er_{2-x}Ca_x)CoO_{4-z}$ did not exist in the CaO-CoO_x-ErO_y system at 885℃. The phase relationship of each solid solution zone will be discussed in detail below.

3.2.1. $(Ca_{3-x}Er_x)Co_4O_{9-z}$

$Ca_3Co_4O_9$ was found in CaO-CoO_x boundary binary system, which is a mismatched layered oxide. $Ca_3Co_4O_9$ has the perovskite-derived structure. $Ca_3Co_4O_9$ is a good thermoelectric material and has a splendid prospect in the field of energy. The solid solution region $(Ca_{3-x}Er_x)Co_4O_{9-z}$ forms with the addition of doping element Er. Ten samples were selected near $Ca_3Co_4O_9$ to explore the boundary of the solid solution region $(Ca_{3-x}Er_x)Co_4O_{9-z}$, with the dopant of Er, the content of x in the solid solution $(Ca_{3-x}Er_x)Co_4O_{9-z}$ was found to be from 0 to 0.9.

3.2.2. $(Ca_{3-x}Er_x)Co_2O_{6-z}$

$Ca_3Co_2O_6$ was found in the CaO-CoO_x boundary binary system, the corresponding Co content is 40 at.%. $Ca_3Co_2O_6$ has the perovskite-derived structure. $Ca_3Co_2O_6$ is a good thermoelectric material and has a splendid prospect in the field of energy. The solid solution region $(Ca_{3-x}Er_x)Co_2O_{6-z}$ forms with the addition of doping element Er, the solid solution formation appears for $(Ca_{3-x}Er_x)Co_2O_{6-z}$, with the value of x ranging from 0 to 1.25. The XRD patterns of the sample with 40 at.% Co content and results of MDI Jade show the peak shift systematically with the Er content. As shown in **Figure 3**, the peaks shift with the amount of Er content in $(Ca_{3-x}Er_x)Co_2O_{6-z}$, but the directions of peak shiftings are not the same. In **Figure 3**, it is seen that the crystal plane (113) moves towards a low angle direction, while the crystal plane (300) moves toward a high angle direction, probably due to anisotropic expansion of the unit cell.

Preprints (www.preprints.org) | NOT PEER-REVIEWED | Posted: 22 May 2023 doi:10.20944/preprints202305.1486.v1

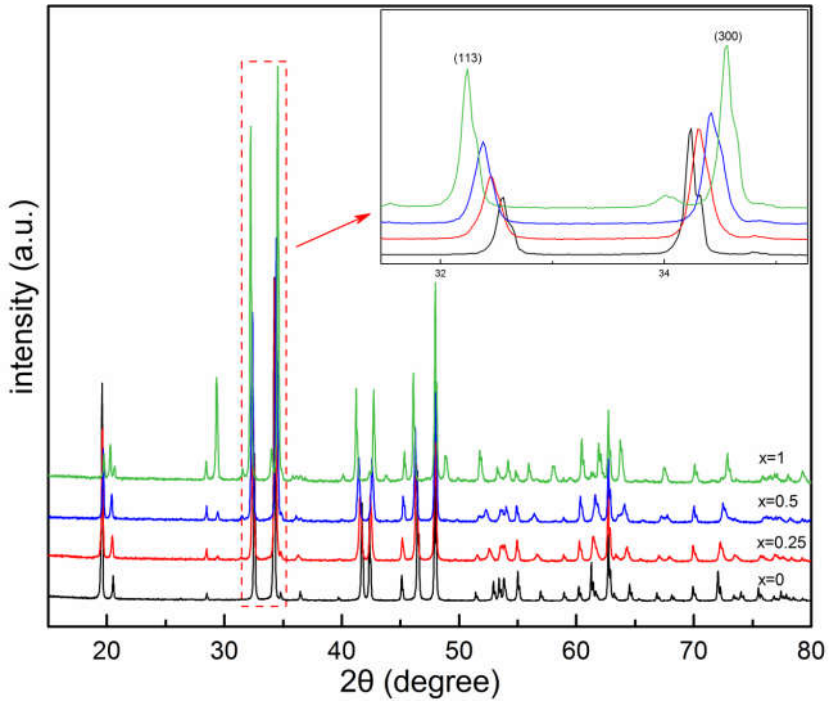

Figure 3. XRD patterns of $(Ca_{3-x}Er_x)Co_2O_{6-z}$ (x=0, 0.25, 0.5, 1).

At 885℃, solid solution was found near $Ca_3Co_2O_6$. The samples $(Ca_{3-x}Er_x)Co_2O_{6-z}$ (x= 0, 0.25, 0.5, 1) were slowly scanned with XRD followed by Rietveld finishing. The diffraction patterns were analyzed by the Rietveld refinement technique using the Fullprof program. **Figure 4** shows the refinement results of $(Ca_2Er_1)Co_2O_{6-z}$ and $Ca_3Co_2O_6$, respectively, with χ^2 of 2.47 and 2.22.

Preprints (www.preprints.org) | NOT PEER-REVIEWED | Posted: 22 May 2023 doi:10.20944/preprints202305.1486.v1

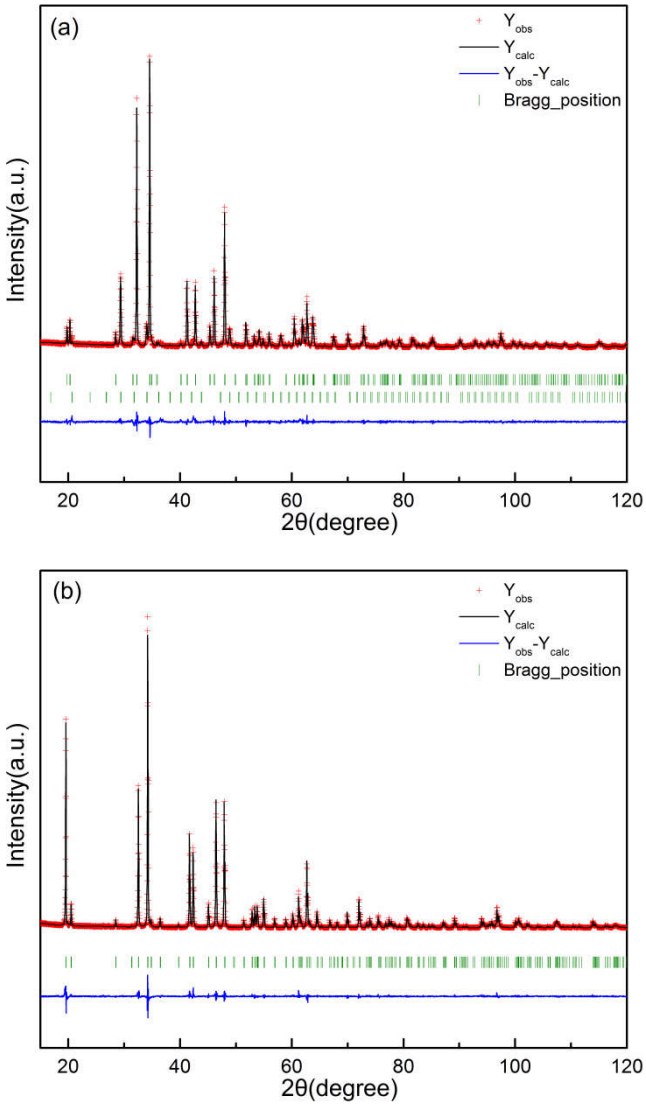

Figure 4. Rietveld analysis results for (a)$(Ca_2Er_1)Co_2O_{6-z}$ and (b)$Ca_3Co_2O_6$. Y_{obs} represents the experimental spectrum, Y_{calc} represents the calculated spectrum, the short vertical line below the diffraction spectrum represents the Bragg diffraction peak position of the corresponding phase, and Y_{obs}-Y_{calc} represents the difference between the experimental spectrum and the calculated spectrum.

Table 2 and **Table 3** provide the refinement parameters and the atomic coordinates of $(Ca_{3-x}Er_x)Co_2O_{6-z}$ (x=0, 0.25, 0.5, 1), respectively. **Figure 5** shows the changes of cell parameters of $(Ca_{3-x}Er_x)Co_2O_{6-z}$ (x=0, 0.25, 0.5, 1). With the increase of x, a and b become smaller and c becomes larger, confirming the previous conjecture.

Preprints (www.preprints.org) | NOT PEER-REVIEWED | Posted: 22 May 2023 doi:10.20944/preprints202305.1486.v1

Table 2. Refinement parameters of $(Ca_{3-x}Er_x)Co_2O_{6-z}$ (x=0, 0.25, 0.5, 1). The bracketed values represent standard deviations.

x	a&b (Å)	c (Å)	Rwp	χ^2
0	9.07628(8)	10.38005(12)	11.0	2.22
0.25	9.05344(21)	10.44059(28)	10.8	3.53
0.5	9.02907(22)	10.50383(28)	9.57	3.43
1	8.98770(12)	10.58704(17)	6.79	2.47

Table 3. Atomic coordinates and displacement parameters for $(Ca_{3-x}Er_x)Co_2O_{6-z}$. The bracketed values represent standard deviation.The numerical error of B_{ios} obtained by XRD is relatively large, so the neutron diffraction B_{ios} [38] is used in the finishing.

	x	y	z	B_{iso} [38]
$Ca_3Co_2O_6$				
Ca	0.36986(2)	0	0.25	0.39
Co1	0	0	0	0.37
Co2	0	0	0.25	0.48
O	0.17804(6)	0.02561(8)	0.11402(5)	0.53
$(Ca_{2.75}Er_{0.25})Co_2O_{6-z}$				
Ca/Er	0.36834(3)	0	0.25	0.39
Co1	0	0	0	0.37
Co2	0	0	0.25	0.48
O	0.17787(11)	0.02463(13)	0.11268(7)	0.53
$(Ca_{2.5}Er_{0.5})Co_2O_{6-z}$				
Ca/Er	0.36773(3)	0	0.25	0.39
Co1	0	0	0	0.37
Co2	0	0	0.25	0.48
O	0.17959(12)	0.02464(14)	0.11238(8)	0.53
$(Ca_2Er_1)Co_2O_{6-z}$				
Ca/Er	0.36688(2)	0	0.25	0.39
Co1	0	0	0	0.37
Co2	0	0	0.25	0.48
O	0.18265(12)	0.02475(13)	0.11010(7)	0.53

Preprints (www.preprints.org) | NOT PEER-REVIEWED | Posted: 22 May 2023 doi:10.20944/preprints202305.1486.v1

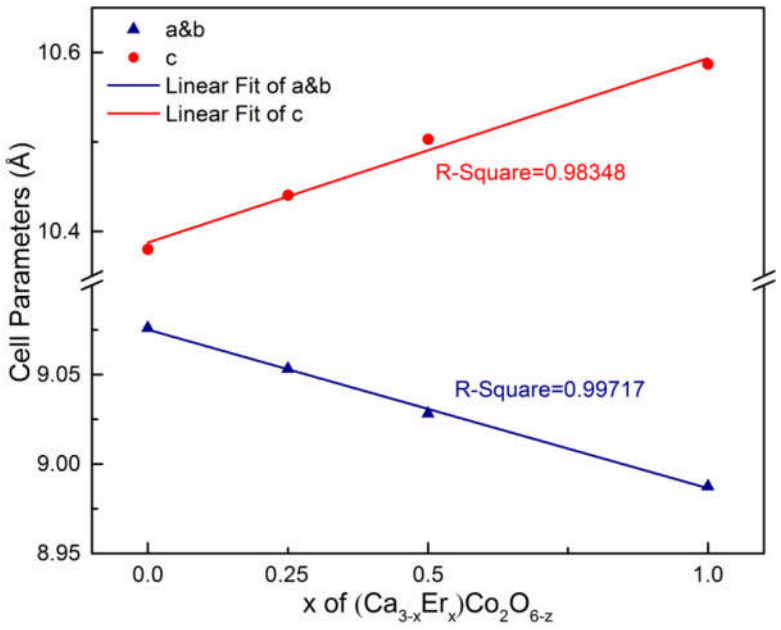

Figure 5. Cell parameters of $(Ca_{3-x}Er_x)Co_2O_{6-z}$ (x=0, 0.25, 0.5, 1).

The Co-O chain in the $Ca_3Co_2O_6$ crystal structure is part of a polyhedron chain parallel to the c axis. **Figure 6** gives the projection of the regular octahedrons and distorted trigonal prisms of the Co-O chain along the b axis. One can construct various planes using neighboring O ions in the Co-O chain; among these planes, the one perpendicular to the c axis was found to move most significantly with the doping of Er. ***Table 4*** gives the structural parameters of $(Ca_{3-x}Er_x)Co_2O_{6-z}$. With the increase of Er content, the $Ca_3Co_2O_6$ structure is lengthened in the c axis direction, mainly due to the lengthening of h2 (shown in **Figure 6**), or the distorted trigonal prism in the Co-O chain is elongated.

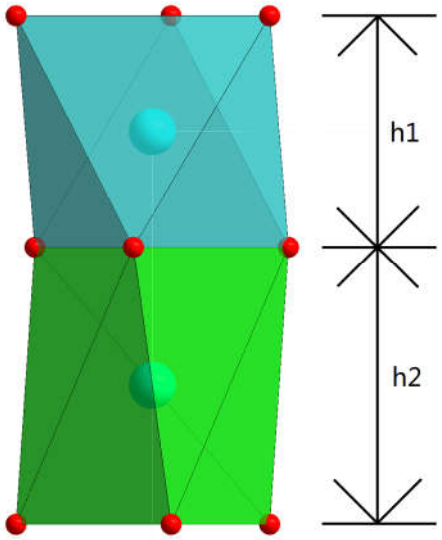

Figure 6. Projection of the regular and distorted octahedron in the Co-O chain along the *b* axis, where h1 is the height of the regular octahedron along the *c* axis and h2 is the height of the distorted trigonal prism along the *c* axis.

Preprints (www.preprints.org) | NOT PEER-REVIEWED | Posted: 22 May 2023 doi:10.20944/preprints202305.1486.v1

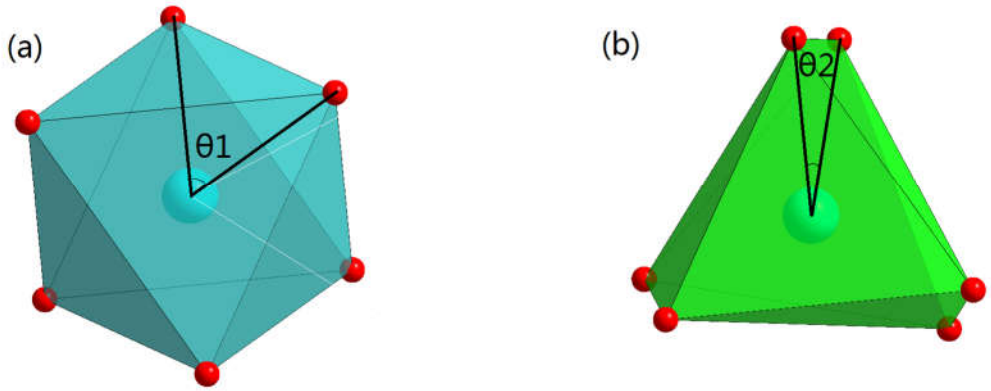

Figure 7. Projection of the regular octahedron (a) and distorted trigonal prism (b) in the Co-O chain along the c-axis, θ1 and θ2 in the figure represent the angles in the projection.

Table 4. Structural parameters of $(Ca_{3-x}Er_x)Co_2O_{6-z}$. In this table, h1 and h2 represent the distance between the planes of oxygen ion perpendicular to the c-axis (**Figure 6**). Columns Occ_{Ca} and Occ_{Er} represent the occupancy of Ca and Er ions, which are in the position of 18e. θ1 and θ2 are the angles in the projection of **Figure 7**, the bracketed values represent standard deviation.

x	h1(Å)	h2(Å)	h1+h2(Å)	Occ_{Ca}	Occ_{Er}	θ1(degree)	θ2(degree)
0	2.367	2.823	5.19	1	0	60.000(44)	15.290(39)
0.25	2.3529	2.8674	5.2203	0.916	0.076	60.000(53)	14.683(52)
0.5	2.3608	2.8911	5.2519	0.834	0.16	60.000(51)	14.540(52)
1	2.3312	2.9623	5.2935	0.666	0.298	60.000(45)	14.349(38)

Ca ion is replaced by Er ion in $(Ca_{3-x}Er_x)Co_2O_{6-z}$ crystal structure. Since Er ion is positive trivalent and Ca ion is positive bivalent, Er^{3+} entering $(Ca_{3-x}Er_x)Co_2O_{6-z}$ structure would be less than Ca^{2+}, and causing site vacancy. In ***Table 4***, Occ_{Ca} and Occ_{Er} represent the occupancy of Ca and Er sites, which are in the position of 18e. Moreover, the radius of Er^{3+} is smaller than that of Ca^{2+} [39], so the entry of Er ion is expected to lead to the shortening of the crystal structure of $(Ca_{3-x}Er_x)Co_2O_{6-z}$ in the direction of *a*&*b*.

In **Figure 3**, the crystal plane (300) can be used to represent the *a*&*b* direction, and the crystal plane (113) can approximately represent the c direction. With the increase of x, the crystal plane (300) moves towards the higher angle direction, which means the crystal structure becomes shorter in the a&b direction, and the crystal plane (113) shifts towards the lower angle direction, which means the crystal structure becomes longer in the c direction.

Figure 7 shows the *c* axis projection of the regular octahedron and distorted trigonal prism in the Co-O chain, and **Table 4** shows the angle of θ in **Figure 7**. The angle θ1 of the regular octahedron is 60°, while the angle θ2 of the distorted trigonal prism is much less than 60°. With the increase of x, angle θ2 tends to become even smaller. This is the reason why the distorted trigonal prism becomes elongated in the direction of the *c* axis.

In conclusion, with the increase of x value in $(Ca_{3-x}Er_x)Co_2O_{6-z}$, the diffraction peak migration direction of $Ca_3Co_2O_6$ in XRD pattern is inconsistent. The structure analysis of $(Ca_{3-x}Er_x)Co_2O_{6-z}$ series samples shows that with the increase of x value, Er ions in the structure of $(Ca_{3-x}Er_x)Co_2O_{6-z}$ increase, and the radius of Er ion is smaller than that of Ca ion, because Er ion is +3 valence and Ca ion is +2 valence, The valence equilibrium makes the number of incoming Er ions less than the number of replaced Ca ions, so the structure of $(Ca_{3-x}Er_x)Co_2O_{6-z}$ is shortened in the *a*&*b* directions; As the x value

Preprints (www.preprints.org) | NOT PEER-REVIEWED | Posted: 22 May 2023 doi:10.20944/preprints202305.1486.v1

increases, the Co-O chain becomes longer, so the structure of $(Ca_{3-x}Er_x)Co_2O_{6-z}$ becomes longer in the *c* direction.

3.2.3. $(Er_{1-x}Ca_x)CoO_{3-z}$

$ErCoO_3$ was found in the CoO_x-ErO_y boundary binary system. $ErCoO_3$ has a perovskite structure, it is a perovskite-type oxide, and it has thermoelectric properties. The solid solution region $(Er_{1-x}Ca_x)CoO_{3-z}$ forms with the addition of doping element Ca. thirteen samples were selected near $ErCoO_3$ to explore the boundary of the solid solution region $(Er_{1-x}Ca_x)CoO_{3-z}$, and the range of x in solution region $(Er_{1-x}Ca_x)CoO_{3-z}$ is from 0 to 0.33.

4. Discussion

It appears that the ionic size of the alkaline-earth and lanthanide ions governs the trend of phase formation, extent of solid solution formation of $(R_{1-x}Ca_x)CoO_{3-z}$, $(R_{1-x}Ca_x)_2O_{3-z}$, $(Ca_{3-x}R_x)Co_4O_{9-z}$ and $(Ca_{3-x}R_x)Co_2O_6$, as well as the tie-line relationships in the CaO-CoO_x-RO_y systems. Because of different phase formation and different range of solid solutions in the La, Dy, and the Er systems, the tie-line relationships are substantially different, leading to different appearance of the diagrams.

Since the doped element R in CaO-CoO_x-RO_y series are lanthanide elements, these diagrams are expected to be related. Therefore, the next step of our present study is to compare the ternary phase diagrams of R=La [28], Dy [33] and Er at 885 ℃. **Figure 8** and **Figure 9** show the CaO-CoO_x-RO_y ternary phase diagrams of R=La and Dy.

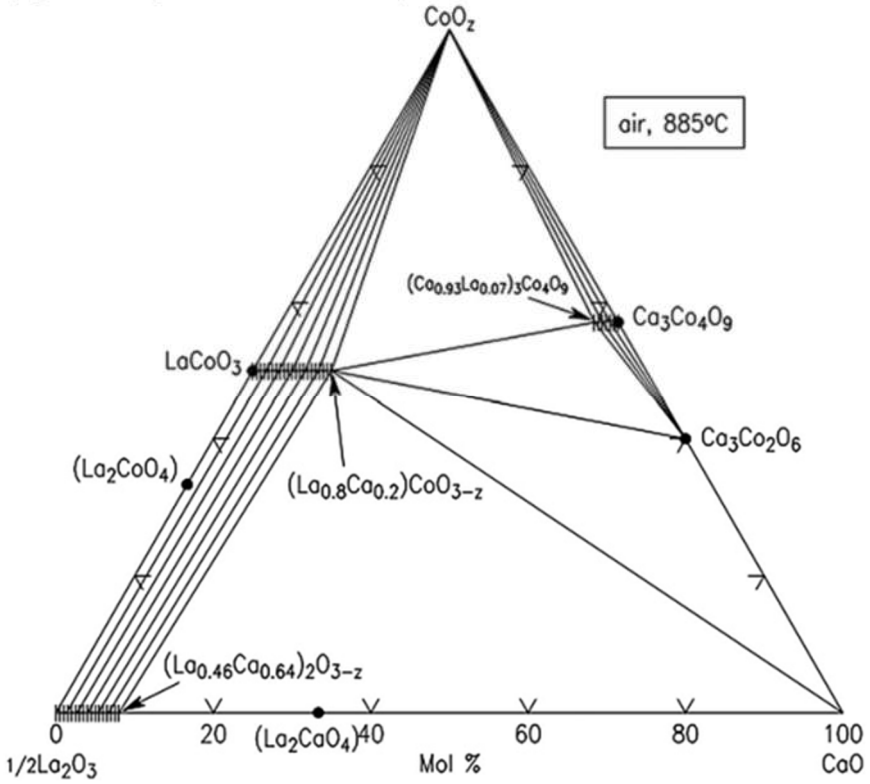

Figure 8. Phase diagram of the CaO-CoO_x-LaO_y system at 885 °C in air [28].

Preprints (www.preprints.org) | NOT PEER-REVIEWED | Posted: 22 May 2023 doi:10.20944/preprints202305.1486.v1

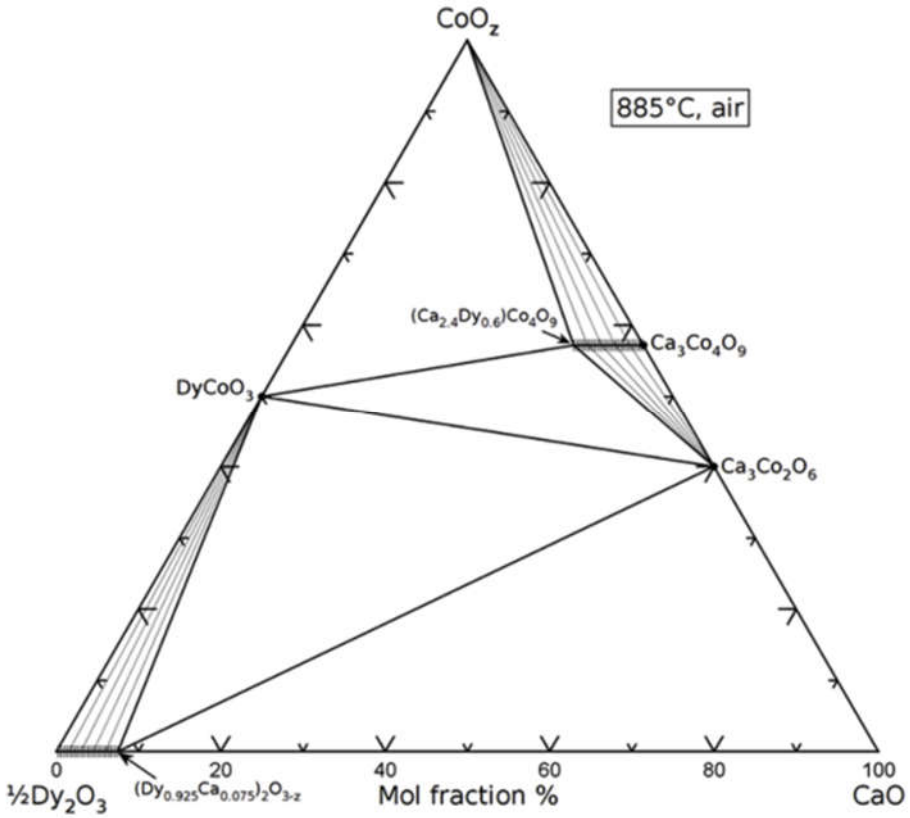

Figure 9. Phase diagram of the CaO-CoO_x-DyO_y system at 885 °C in air [33].

La is the first element in the lanthanide series, and CaO-CoO_x-LaO_y [28] is the first phase diagram of CaO-CoO_x-RO_y (R is lanthanide) series at 885℃, therefore CaO-CoO_x-LaO_y has provided a guide for the entire series of phase diagrams. The phase diagrams of CaO-CoO_x-LaO_y and CaO-CoO_x-ErO_y were compared. The solid solution regions of $(Ca_{3-x}R_x)Co_4O_{9-z}$ and $(R_{1-x}Ca_x)CoO_{3-z}$ existed in both systems. Although both systems contain perovskite $RCoO_3$ phase, $LaCoO_3$ and $ErCoO_3$ have different structures. $LaCoO_3$ phase is rhombohedral and with a space group of R-3c [28], while $ErCoO_3$ phase is orthorhombic with space group Pnma. The difference in size of lanthanide ions ($rLa^{3+}>rCa^{2+}>rEr^{3+}$) [39] results in the different structures of $LaCoO_3$ and $ErCoO_3$. In the CaO-CoO_x-LaO_y system in air at 885 ℃, there is no solid solution phenomenon near $Ca_3Co_2O_6$, which is different from the CaO-CoO_x-ErO_y system in air at 885 ℃. And in the CaO-CoO_x-LaO_y system in air at 885 ℃, there is a solid solution phenomenon near La_2O_3, which is different from the CaO-CoO_x-ErO_y system in air at 885 ℃.

In the phase diagram of the CaO-CoO_x-DyO_y and CaO-CoO_x-ErO_y systems, only one solid solution region is the same, namely $(Ca_{3-x}R_x)Co_4O_{9-z}$, but the range of the two solid solution regions is different when R=Dy, 0≤x≤0.6, and R=Er, 0≤x≤0.9. $(Ca_{3-x}Er_x)Co_2O_{6-z}$ is a new solid solution region, and other CaO-CoO_x-RO_y (R is lanthanide element) phase diagrams do not show solid solution phenomenon at $Ca_3Co_2O_6$ at 885 ℃.Because of the different phase formation of these three systems, the tie-line relationships are also very different. In the La system, there are four three-phase regions and four two-phase connecting tie-line bundles [28]. In the Dy system, there are four three-phase regions and three two-phase connecting the tie-line bundles [33]. In the Er system, however, due to the addition of the $(Ca_{3-x}Er_x)Co_2O_{6-z}$ phase, there are four three-phase regions and five solid solution tie-line regions.

5. Conclusions

The phase diagram of CaO-CoO_x-ErO_y system at 885℃ has been drawn. This phase diagram shows the phase relationships between the phases in the CaO-CoO_x-ErO_y ternary system, which is crucial for knowing and understanding the properties and properties of the materials in the system. There are four three phase zones and five solid solution contact zones in the system. Three series of

solid solutions have been found in the CaO-CoO_x-ErO_y system at 885℃, which are respectively ($Er_{1-x}Ca_x$)CoO_{3-z} (0≤x≤0.33) with simple perovskite structure, and ($Ca_{3-x}Er_x$)Co_4O_{9-z} (0≤x≤0.9) and ($Ca_{3-x}Er_x$)Co_2O_{6-z} (0≤x≤1.25) with perovskite-derived structures. The solid solution phenomenon will lead to changes in the structure of materials, which will lead to changes in the properties and properties of materials. The solid solution of perovskite and its derived structure in the system will affect the properties of materials. Studying the structure of materials will help to understand the changes in material properties, and help to explore the acquisition of materials with more efficient energy conversion and storage. The solid solution is formed near $Ca_3Co_2O_6$. With the increase of x value in ($Ca_{3-x}Er_x$)Co_2O_{6-z}, the diffraction peak migration direction of $Ca_3Co_2O_6$ in XRD pattern is inconsistent. The structural analysis of ($Ca_{3-x}Er_x$)Co_2O_{6-z} series samples concludes that this difference is the anisotropic expansion of the unit cell.

Author Contributions: Conceptualization, HaoCheng Wang, HaoMing Ning, ZhenJun Fan, GuangYao Liu; resources, ZhenJun Fan, GuangYao Liu; writing original draft preparation, HaoCheng Wang, HaoMing Ning; preparing figures, HaoCheng Wang, HaoMing Ning; review and editing, ZhenJun Fan, GuangYao Liu. All authors have read and agreed to the published version of the manuscript.

Funding: This work was supported by the Chinese Academy of Sciences Strategic Priority Research Program B (Grant No. XDB07010300) and the National Natural Science Foundation of China (Grant No. 11674376).

Data Availability Statement: The data that support the findings of this study are available on request from the corresponding author upon reasonable request.

Conflicts of Interest: The authors declare no conflict of interest.

References

1. Xiao Z.W.; Song Z.N.; Yan Y.F. From Lead Halide Perovskites to Lead-Free Metal Halide Perovskites and Perovskite Derivatives. *Adv Mater.* **2019**, *31(47)*, pp. 1803792. DOI: 10.1002/adma.201803792
2. Shen L.N.; Chen R.; Zhang D.; et al. High-Performance Perovskite Photovoltaics by Heterovalent Substituted Mixed Perovskites. *Adv. Funct. Mater.* **2022**, *32(47)*, pp. 2207911. DOI: 10.1002/adfm.202207911
3. Wang J.F.; Luo S.Q.; Lin Y.; et al. Templated growth of oriented layered hybrid perovskites on 3D-like perovskites. *Nat Commun*. **2020**, *11*, pp. 582. DOI: 10.1038/s41467-019-13856-1
4. Mohapatra A.; Singh N.; Singh A.; et al. Solution-Processed Perovskite/Perovskite Heterostructure Via a Grafting-Assisted Transfer Technique. *ACS Appl Energy Mater*. **2021**, *4(2)*, pp. 1962-1971. DOI: 10.1021/acsaem.0c03086
5. Clark C.P.; Mann J.E.; Bangsund J.S.; et al. Formation of Stable Metal Halide Perovskite/Perovskite Heterojunctions. *ACS Energy Lett*. **2020**, *5(11)*, pp. 3443-3451. DOI: 10.1021/acsenergylett.0c01609
6. Riffat S.B.; Ma X. Thermoelectrics: a review of present and potential applications. *Appl Therm Eng*. **2003**, *23(8)*, pp. 913-935. DOI: 10.1016/S1359-4311(03)00012-7
7. Ma Z.; Wei J.T.; Song P.S.; et al. Review of experimental approaches for improving zT of thermoelectric materials. *Mat Sci Semicon Proc*. **2021**, *121*, pp. 105303. DOI: 10.1016/j.mssp.2020.105303
8. Zhang S.H.; Niu X.B.; Xie Y.Q.; et al. High intrinsic ZT in InP_3 monolayer at room temperature. *J Phys-Condens Mat*. **2019**, *31*, 365501. DOI: 10.1088/1361-648x/ab249b
9. Fjellva G.H.; Gulbrandsen E.; Aasland S.; et al. Crystal Structure and Possible Charge Ordering in One-Dimensional $Ca_3Co_2O_6$. *J Solid State Chem.* **1996**, *124(1)*, pp. 190-194. DOI: 10.1006/jssc.1996.0224
10. Hardy V.; Flahaut D.; Fresard R.; et al. Anisotropic susceptibility of the geometrically frustrated spin-chain compound $Ca_3Co_2O_6$. *J Phys-Condens Mat.* **2007**, *19(14)*, pp. 1898-1908. DOI: 10.1088/0953-8984/19/14/145229
11. Hardy V.; Lees M.R.; Petrenko O.A.; et al. Temperature and time dependence of the field-driven magnetization steps in $Ca_3Co_2O_6$ single crystals. *Phys Rev B.* **2004**, *70(6)*, pp. 064424. DOI: 10.1103/PhysRevB.70.064424
12. Masset A.C.; Michel C.; Maignan A.; et al. Misfit-layered cobaltite with an anisotropic giant magnetoresistance: $Ca_3Co_4O_9$. *Phys Rev B.* **2000**, *62(1)*, 166-175. DOI: http://dx.doi.org/10.1103/PhysRevB.62.166
13. Kenfaui D.; Chateigner D.; Gomina M.; et al. Texture, mechanical and thermoelectric properties of $Ca_3Co_4O_9$ ceramics. *J Appl Ceram Tec.* **2009**, *490(1)*, pp. 472-479. DOI: 10.1016/j.jallcom.2009.10.048
14. Saini S.; Yaddanapudi H.S.; Tian K.; et al. Terbium Ion Doping in $Ca_3Co_4O_9$: A Step towards High-Performance Thermoelectric Materials. *Sci Rep.* **2017**, *7*, pp. 44621. DOI: 10.1038/srep44621
15. Ren G.K.; Lan J.L.; Zhao L.D.; et al. Layered oxygen-containing thermoelectric materials: Mechanisms, strategies, and beyond. *Mater. Today* **2019**, *29*, pp. 68-85. DOI: 10.1016/j.mattod.2019.07.003

16. Tanabe K.; Okazaki R.; et al. Optical conductivity of layered calcium cobaltate $Ca_3Co_4O_9$. *J Phys-Condens Mat.* **2016**, *085601*. DOI: 10.1088/0953-8984/28/8/085601
17. Li S.W.; Funahashi R.; Matsubara I.; et al. Synthesis and thermoelectric properties of the new oxide ceramics $Ca_{3-x}Sr_xCo_4O_{9+\delta}$ (x=0.0-1.0). *Ceram Int.* **2001**, *27(3)*, pp. 321-324. DOI: 10.1016/s0272-8842(00)00083-3
18. Bhattacharya S.; Aswal D.K.; Singh A.; et al. Anisotropic electrical transport studies of $Ca_3Co_4O_9$ single crystals grown by the flux method. *J Cryst Growth.* **2005**, *277(1-4)*, pp. 246-251. DOI: 10.1016/j.jcrysgro.2004.12.142
19. Wolf M.; Rehder L.; Steinbach F.; et al. Combination of Laser and Thermal Sintering of Thermoelectric $Ca_3Co_4O_9$ Films. *Chem Ing Tech*. **2021**, *94(1)*, pp. 177-185. DOI: 10.1002/cite.202100128
20. Li Y.N.; Wu P.; Zhang S.P.; Pei Y.L.; et al. Enhanced thermoelectric properties of $Ca_3Co_4O_9$ by adding nano $MoSi_2$. *Ceram Int*. **2022**, *48(22)*, pp. 33967-33975. DOI: 10.1016/j.ceramint.2022.07.346
21. Terasaki I.; Sasago Y.; et al. Large thermoelectric power in $NaCo_2O_4$ single crystals. *Phys Rev B*. **1997**, *56(20)*, R12685–R12687. DOI: 10.1103/PhysRevB.56.R12685
22. Wang S.F.; Venimadhav A.; Guo S.M.; et al. Structural and thermoelectric properties of $Bi_2Sr_2Co_2O_y$ thin films on $LaAlO_3$ (100) and fused silica substrates. *Appl Phys Lett.* **2009**, *94(2)*, pp. R12685. DOI: 10.1063/1.3072803
23. Wong-Ng W.; Yan Y.; Kaduk J.A.; Tang X.F. X-ray powder diffraction reference patterns for $Bi_{1-x}Pb_{(x)}OCuSe$. *Power Diffr*. **2006**, *0885*. DOI: 10.1017/s0885715616000361
24. Wong-Ng W.; Liu G.Y.; Martin J.; et al. Phase compatibility and thermoelectric properties of compounds in the Sr–Ca–Co–O system. *J Appl Phys.* **2010**, *107(3)*, pp. 188-488. DOI: 10.1063/1.3276158
25. Wong-Ng W.; Luo T.; Xie W.; et al. Phase diagram, crystal chemistry and thermoelectric properties of compounds in the Ca-Co-Zn-O system. *J Solid State Chem*. **2011**, *184(8)*, pp. 2159-2166. DOI: 10.1016/j.jssc.2011.06.013
26. Li S.W.; Funahashi R.; Matsubara I.; et al. Synthesis and Thermoelectric Properties of the New Oxide Materials $Ca_{3-x}Bi_xCo_4O_{9+\delta}$ ($0.0 < x < 0.75$). *Chem Mater.* **2000**, *31(47)*, pp. 2424-2427. DOI: 10.1021/cm000132r
27. Thorogood G.J.; Orain P.Y.; Ouvry M.; Piriou B.; Tedesco T.; Wallwork K.S.; Herrmann J.; James M. Structure, crystal chemistry and magnetism of rare earth calcium-doped cobaltates: $Ln_{2-x}Ca_xCoO_{4+\delta}$ (Ln= Pr, Nd, Sm, Eu and Gd). *Solid State Sci.* **2011**, *13(12)*, pp. 2113-2123. DOI: 10.1016/j.solidstatesciences.2011.08.008
28. Wong-Ng W.; Laws W.J.; Yan Y.G. Phase diagram and crystal chemistry of the La-Ca-Co-O system. *Solid State Sci.* **2013**, *17*, pp. 107–110. DOI: 10.1016/j.solidstatesciences.2012.11.021
29. Wong-Ng W.; Laws W.J.; Lapidus S.H.; et al. Phase equilibria and crystal chemistry of the CaO-Nd_2O_3-CoO_z system at 885°C in air. *Solid State Sci.* **2014**, *215*, pp. 128-134. DOI: 10.1016/j.jssc.2014.03.012
30. Wong-Ng W.; Laws W.J.; Lapidus S.H.; et al. Phase equilibria and crystal chemistry of the CaO-Sm_2O_3-CoO_z system at 885°C in air. *Solid State Sci.* **2015**, *48*, pp. 31-38. DOI: 10.1016/j.solidstatesciences.2015.06.003
31. Wong-Ng W.; Laws W.J.; Kaduk J.A. Crystal chemistry and phase equilibria of the CaO-Eu_2O_3-CoO_z system at 885°C in air. *Solid State Sci.* **2016,** *2558(16)*, pp. 30391. DOI: 10.1016/j.solidstatesciences.2016.06.007
32. Wong-Ng W.; Laws W.J.; Lapidus S.H.; et al. Phase equilibria and crystal chemistry of the CaO-Gd_2O_3-CoO_z system at 885°C in air. *Solid State Sci.* **2017**, *72*, pp. 128-134. DOI: 10.1016/j.solidstatesciences.2017.08.005.
33. Wong-Ng W.; Laws W.J.; Kaduk J.A. Crystal chemistry and phase equilibria of the CaO-Dy_2O_3-CoO_z system at 885°C in air. *Solid State Sci.* **2018**, *88*, pp. 57-62. DOI: 10.1016/j.solidstatesciences.2018.12.010
34. Wong-Ng W.; Laws W.J.; Huang Q.; et al. Crystal chemistry and phase equilibria of the CaO-Ho_2O_3-CoO_z system at 885°C in air. *Solid State Sci.* **2020**, *107*, pp. 106348. DOI: 10.1016/j.solidstatesciences.2020.106348
35. Gates-Rector S.D.; Blanton T.N. The Powder Diffraction File: A quality Materials Characterization Database. *Powder Diffr.* **2019**, *34*, pp. 352–360.
36. Rietveld H.M. A method for including the line profiles of neutron powder diffraction peaks in the determination of crystal structures. *Acta Crystallogr.* **1966**, *229*, pp. 151.
37. Rodriguez-Carvajal J.L. Recent advances in magnetic structure determination by neutron powder diffraction. *Physica B.* **1993**, *19255*. DOI:10.1016/0921-4526(93)90108-I.
38. Jain A.; Singh S.; Yusuf S.M. Structural and magnetic properties of spin chain compounds $Ca_3Co_{2-x}Fe_xO_6$, *Phys.Rev.B* **2006**, *74* pp. 174419. DOI:10.1103/PhysRevB.74.174419.
39. Shannon R.D. Revised Effective Ionic Radii and Systematic Studies of Interatomie Distances in Halides and Chaleogenides. *Acta Cryst.* **1976**, *A32*, pp. 751-767. DOI:10.1107/S0567739476001551.